HYBRID FINITE-VOLUME/DISCONTINUOUS GALERKIN FRAMEWORK FOR THE SOLUTION OF MULTIPHYSICS PROBLEMS USING UNSTRUCTURED MESHES

V. Maltsev[1], P. Tsoutsanis[1], M. Skote[1]

[1] School of Aerospace, transport and Manufacturing
Cranfield University,
Cranfield MK43 0AL, United Kingdom,
email: v.maltsev@cranfield.ac.uk, panagiotis.tsoutsanis@cranfield.ac.uk,
m.skote@cranfield.ac.uk

Key words: Multi-Species flows, Finite Volume, Discontinuous Galerkin, Diffuse Interface Models

Abstract. A hybrid FV/DG framework is developed for the simulation of compressible multi-species flows on unstructured meshes with a five-equation Diffuse-Interface Model [1]. The high order DG method is employed for the purpose of limiting the material interface smearing typical of the diffuse-interface models resulting from excessive numerical dissipation [2, 3]. In order to ensure high-order accuracy in smooth flow regions and non-oscillatory behaviour near shocks or material interfaces, the hybrid scheme resorts to the underlying FV method when invalid cells are detected by a troubled cell indicator checking the unlimited DG solution, and enables a high-order non-linear CWENOZ reconstruction [4,5] if the solution present oscillations. The CWENO and CWENOZ type reconstruction uses a high-order polynomial for the central stencil and a lower-order polynomial for the directional stencils enhancing robustness and efficiency of classic WENO schemes. To achieve consistency in advecting material interfaces at constant pressure and velocity, the source term from the non-conservative equation is discretised compatibly with the Riemann solver, following the work of Johnsen and Colonius [6].

1 INTRODUCTION

The simulation of multi-species flows in compressible medium is of growing interest in the CFD community as these kind of flows can be encountered in many areas of science and engineering. Physically, the material interface separating two different phases or species is in the order of nanometers, however, the way it is approximated differentiates the main methods developed for simulating such flows. In an Eulerian framework, two main classes became popular for simulating multi-species flows: the Sharp Interface Methods (SIM), and the Diffuse Interface Methods (DIM). SIM treats the interface as infinitely thin and does not allow fluid mixing at the interface, and includes several subcategories such the volume-of-fluid (VOF) [7] and the level-set-method [8,9], which are well established in the context of incompressible flows. In this context, the Lagrangian front tracking method has also to be mentioned [10, 11]. On the other hand, the DIM treats the material interface as a diffused zone and allows the artificial mixing of the species in proximity of the interface. A plethora of models were developed

on this assumption, first of which the seven-equation model of Baer and Nunziato [12] for the detonation-to-deflagration transition in granular materials, and following, the four-equation model of Abgrall [13] with interface-equilibrium condition (IEC) for the simulation of two-ideal gases, the reduced five-equation model of Kapila et al. [14], and the five-equation model of Allaire et al. [1] with isobaric closure for the simulation of two-phase flows. Many other models were derived, accounting for additional physical features, such the unified hyperbolic formulation of Godunov-Peshkov-Romenskij (GPR model) [15, 16] and the elasto-plastic and visco-plastic models of Favrie and Gavrilyuk [17, 18]. DIM are easier to be implemented compared to SIM as the same set of equation is applied everywhere in the domain, and in the context of compressible flows they are more robust in enforcing discrete conservation. In the present work, the five-equation model of Allaire is adopted.

The drawback of adopting a DIM is the increasing interface smearing due to numerical dissipation, and thus requires a careful calibration of the spatial discretisation, or, as proposed by So et al. [19], Shuckla et al. [20], and Tiwari et al. [21], can be counteracted by the introduction of regularization terms to counteract for the interface dissipation. In this work we will investigate in that sense the performance of a high-order spatial discretisation, through a hybrid Discontinuous Galerkin (DG) and a high-order Finite Volume (FV) scheme. The DG method is well known for its accuracy and is nowadays a typical candidate for high-order methods, although computationally demanding and non-trivial for the treatment of non-conservative terms. DIM generally contain at least one equation written in non-conservative form that accounts for the volume fraction advection. Path-conservative [22] and Local DG [23] techniques have been applied to account for non-conservative terms. Our strategy will take advantage of the discretisation introduced by Johnsen and Colonius [6], where the source term is treated as a surface integral and the volume fraction from the bulk flow is used. Potential oscillations in the solution resulting from material or other discontinuities are detected by a troubled cell indicator checking the unlimited DG solution. For the cells deemed as troubled the hybrid scheme will resort to the high-order CWENOZ [5, 24] reconstruction of the underlying FV thus ensuring high-order accuracy in smooth regions and non-oscillatory behaviour in presence of shocks or material interfaces. The implementation is performed within the open-source Unstructured Compressible Navier-Stokes (UCNS3D) [25, 26] code.

2 GOVERNING EQUATIONS

The diffuse-interface model used in this work is the quasi-conservative five-equation model of Allaire et al. [1] and consists of two continuity equations Eq.(1) and Eq.(2), a momentum equation per dimension Eq.(3), an energy equation Eq.(4), and the non-conservative advection equation of the volume fraction of one of the two fluids Eq.(5) as given below:

$$\frac{\partial(a_1\rho_1)}{\partial t} + \nabla \cdot (a_1\rho_1\mathbf{u}) = 0, \tag{1}$$

$$\frac{\partial(a_2\rho_2)}{\partial t} + \nabla \cdot (a_2\rho_2\mathbf{u}) = 0, \tag{2}$$

$$\frac{\partial\rho\mathbf{u}}{\partial t} + \nabla \cdot (\rho\mathbf{u}\mathbf{u} + p\mathbf{I}) = 0, \tag{3}$$

$$\frac{\partial E}{\partial t} + \nabla \cdot (E + p)\mathbf{u} = 0, \tag{4}$$

$$\frac{\partial a_1}{\partial t} + \mathbf{u} \cdot \nabla a_1 = 0, \tag{5}$$

where ρ is the density, $\mathbf{u} = (u, v, w)^T$ is the velocity, p is the pressure, E is the total energy and a is the volume fraction. The widely used stiffened gas EOS is employed for closing the five-equation model. It has been primarily selected due to its application for flow problems involving gases, liquids and solids. The stiffened gas EOS characterises each fluid pressure as:

$$p_i = (\gamma_i - 1)\rho_i \epsilon_i - \gamma_i \pi_{\infty,i}, \tag{6}$$

where $\pi_{\infty,i} \geq 0$ is a reference pressure, and will be set to $\pi_\infty = 0$ for gases. The total mass and $\rho\epsilon$ being given by:

$$\rho = \sum_i a_i \rho_i, \tag{7}$$

and $\rho\epsilon$ being

$$\rho\epsilon = \sum_i a_i \rho_i \epsilon_i, \tag{8}$$

where ϵ is the internal energy, with $\rho\epsilon = E - \frac{1}{2}\rho\mathbf{uu}$. The EOS of the mixture reads

$$\xi = \frac{1}{\gamma - 1} = \sum_i \frac{a_i}{\gamma_i - 1}, \tag{9}$$

$$\frac{\pi_\infty \gamma}{\gamma - 1} = \sum_i a_i \frac{\pi_{\infty,i} \gamma_i}{\gamma_i - 1}, \tag{10}$$

$$p = (\gamma - 1)\rho\epsilon - \gamma\pi_\infty, \tag{11}$$

3 NUMERICAL FRAMEWORK

3.1 Conservative Equations

The first four equations of Allaire's model as in Eqs.1 to 4, which are written in conservative form, are solved with a modal DG scheme [27, 28]. For the DG discretisation, the weak form of the above equation has to considered, and is obtained by the multiplication with a smooth test function $\phi(x)$, integrating over the domain Ω and performing an integration by parts. This results in:

$$\int_\Omega \phi(x, y, z)\frac{\partial \mathbf{U}}{\partial t}d\Omega + \oint_{\partial\Omega} \phi(x, y, z)\mathbf{F}(\mathbf{U}) \cdot \mathbf{n}dS = \int_\Omega \nabla\phi(x, y, z) \cdot \mathbf{F}(\mathbf{U})d\Omega. \tag{12}$$

The solution is discretely approximated by a collection of piecewise solution, and on each element those are defined as a combination of n local polynomial basis functions $P(x, y, z)$. The discrete solution lies in a finite-element space of discontinuous functions, i.e. a Sobolev space [29] $V_h = \{\phi_h \in L^\infty : \phi_h|_\Omega \in V^k(\Omega), k = 0, 1, 2, ..., N\}$, where V^k is the space of polynomials of degree up to k. The discrete solution $U_h(x, y, z)$, with expansion coefficients denoted by u_h, can be seen

as expansions over a finite element basis P_j^k in the aforementioned polynomial space, where d is the number of degrees of freedom:

$$U_h(x,y,z,t) = \sum_{j=1}^{d} \mathbf{u}_h(t) P_j^k(x,y,z). \tag{13}$$

The basis function is here a modal cell-centered Taylor expansion truncated to the desired accuracy:

$$P_j^k(x,y,z)|_{\Omega_l} = \frac{(x-x_{c_l})^{p_i}}{h_l^{p_i}} \frac{(y-y_{c_l})^{q_i}}{h_l^{q_i}} \frac{(z-z_{c_l})^{r_i}}{h_l^{r_i}} - \frac{1}{|\Omega_l|} \int_{\Omega_l} \frac{(x-x_{c_l})^{p_i}}{h_l^{p_i}} \frac{(y-y_{c_l})^{q_i}}{h_l^{q_i}} \frac{(z-z_{c_l})^{r_i}}{h_l^{r_i}} d\Omega_l \tag{14}$$

where $0 \leq p_i + q_i + r_i \leq k$ and l ranges over the total number of elements. The normalisation coefficient h, used to improve the mass matrix conditioning, is taken as the square root of target cell's volume [30]. It is convenient to express the integrals of Eq.(12) in terms of an element E of the domain, that in this work will be allowed to be of an arbitrary shape. In order to account for arbitrary shaped elements, in 2D quadrilateral elements are decomposed to triangular elements [31]. The boundary integral will be included in the summation over the faces f of the element E, with total number of faces N_f, and the test function is taken from the same polynomial space of the solution expansion $\phi_h(x,y,z) = \sum_{j=1}^{d} P_j^k(x,y,z)$ and the semi-discrete form will therefore read:

$$\frac{d}{dt} \int_E P_i^k P_j^k \mathbf{u}_h d\Omega + \sum_{f \in \partial E}^{N_f} \oint_f P_j^k \mathbf{F}(\mathbf{U}_h) \cdot \mathbf{n} dS = \int_E \nabla P_j^k \cdot \mathbf{F}(\mathbf{U}_h) d\Omega. \tag{15}$$

The volume integral on the right hand side of Eq.(15) and the surface integral on the left hand side can be calculated by an appropriate Gaussian quadrature rule. Referring with L and M, and with ω_j and ψ_l, to the total number of surface and volume quadrature points and weights respectively, Eq.(15) is approximated with:

$$\frac{d}{dt} \int_E P_i^k P_j^k \mathbf{u}_h d\Omega = \sum_{m=1}^{M} \omega_j \mathbf{F}(\mathbf{U}_h(x_{E,m})) \cdot \nabla P_j^k(\mathbf{x}_{E,m})|E|-$$
$$\sum_{f \in \partial E}^{N_f} \sum_{l=1}^{L} \psi_l \tilde{\mathbf{F}}(\mathbf{U}_h^L(\mathbf{x}_{f,l}), \mathbf{U}_h^R(\mathbf{x}_{f,l})) \cdot \mathbf{n} P_j^k(\mathbf{x}_{f,l})|f| \tag{16}$$

where $\tilde{F}$ is the intercell numerical flux. For the inviscid fluxes the approximate HLLC (Harten-Lax-van Leer-Contact) Riemann solver of Toro [32] is employed, unless otherwise stated. The temporal discretisation employs the 3rd-order explicit Strong Stability Preserving (SSP) Runge-Kutta method [33] which is stable for $CFL \leq 1$. All the volume/surface/line integrals are approximated by Gaussian quadrature rule suitable for the order of polynomial employed.

3.2 Non-conservative equation

The volume fraction advection equation Eq.(5) is written in non-conservative form, and requires a careful treatment. The volume fraction advection Eq.(5) is rewritten in a mathematically

equivalent form as introduced by Johnsen and Colonius [6]:

$$\frac{\partial a_1}{\partial t} + \nabla \cdot (a_1 \mathbf{u}) = a_1 \nabla \cdot \mathbf{u}. \tag{17}$$

The term on the RHS of Eq.(17) is treated as a source term and following the approach of Johnsen and Colonius [6] it is numerically approximated as surface integral, rather than a volume one, while using the same velocity estimate as the one used for the evaluation of the fluxes as shown below:

$$\int_{V_i} \mathbf{s} \, dV \approx \int_{V_i} a_1 \, dV \cdot \int_{\partial V_i} (u_n)^{Riem.} \, dS. \tag{18}$$

Therefore, the discrete form for the non conservative equation reads:

$$\frac{d}{dt} \int_E P_i^k P_j^k \mathbf{u}_h d\Omega = \sum_{m=1}^{M} \omega_j \mathbf{F}(\mathbf{U}_h(\mathbf{x}_{E,m})) \cdot \nabla P_j^k(\mathbf{x}_{E,m})|E| -$$

$$\sum_{f \in \partial E}^{N_f} \sum_{l=1}^{L} \psi_l \tilde{\mathbf{F}}(\mathbf{U}_h^L(\mathbf{x}_{f,l}), \mathbf{U}_h^R(\mathbf{x}_{f,l})) \cdot \mathbf{n} P_j^k(\mathbf{x}_{f,l}) - \mathbf{a}_{i,1}^n \cdot u_n^{Riem}(\mathbf{x}_{f,l}))|f| \tag{19}$$

3.3 Reconstruction

The FV component of the present algorithm used in `UCNS3D` [25, 26] follows the approaches of Tsoutsanis et al. [5, 24, 31, 34], Titarev et al. [35] that have been previously applied to smooth and discontinuous flow problems [5, 24, 25, 31, 34–52]. The CWENOZ scheme in particular employed in this study follows the implementation of Tsoutsanis and Dumbser [5] and is the combination of an optimal (high-order) polynomial p_{opt} with lower-order polynomials. The optimal polynomial uses the central stencil, while the lower-order polynomials employ the directional stencils. When the variation of the solution is smooth, the optimal polynomial is recovered and therefore the desired-order of accuracy is obtained. In the presence of discontinuous data, at least one of the lower-order polynomials arising from the directional stencils could contain smooth data, hence essentially reducing the oscillations in the computed solution, which is of great importance in situations of shock interaction with material interfaces. All the polynomials involved satisfy the requirement of matching the cell averages of the solution, therefore they are solved with the same constrained least-squares technique. The directional stencils employ the Type3 definition which includes one directional stencil per element face as detailed in the work by Tsoutsanis [51]. The optimal polynomial is defined as follows:

$$p_{opt}(x, y, z) = \sum_{s=1}^{s_t} \lambda_s p_s(x, y, z), \tag{20}$$

where s is the stencil index, with $c = 1$ being the central, $c = 2, 3, ...$ being the directional, s_t being the total number of stencils, and λ_s being the linear coefficients for each stencil, whose sum is equal to 1. The p_1 polynomial is not computed directly, but computed by subtracting the lower-order polynomials from the optimum polynomial as follows:

$$p_1(x, y, z) = \frac{1}{\lambda_1} \left(p_{opt}(x, y, z) - \sum_{s=2}^{s_t} \lambda_s p_s(x, y, z) \right). \tag{21}$$

The CWENOZ reconstruction polynomial is given as a non-linear combination of all the polynomials in the following manner:

$$p(x, y, z)^{\text{cwenoz}} = \sum_{s=1}^{s_t} \omega_s p_s(x, y, z), \tag{22}$$

where ω_s correspond to the non-linear weights assigned to each polynomial, and in regions with smooth data $\omega_s \approx \lambda_s$, hence obtaining the high-order approximation from the central stencil, and in regions of discontinuous solutions the reconstructed solution will be mostly influenced from the lower-order polynomials of the directional stencils. The WENOZ component of combining unequal degree polynomials as introduced by Borges et al. and Castro et al. [4,53] is employed in this study, but adapted for unequal polynomials. The non-linear weights are now defined as:

$$\omega_s = \frac{\tilde{\omega}_s}{\sum\limits_{s=1}^{s_t} \tilde{\omega}_s} \quad \text{where} \quad \tilde{\omega}_s = \lambda_s \left(1 + \frac{\tau}{\epsilon + \mathcal{SI}_s} \right). \tag{23}$$

With τ being the universal oscillation indicator and taken as the absolute difference between the smoothness indicators as follows:

$$\tau = \left(\frac{\sum\limits_{s=2}^{s_t} |\mathcal{SI}_s - \mathcal{SI}_1|}{s_t - 1} \right)^b. \tag{24}$$

Similarly to the WENO scheme $\epsilon = 10^{-6}$ is used and $b = 4$. The smoothness indicator $\mathcal{SI}_m$ is given by:

$$\mathcal{SI}_s = \sum_{1 \leq |\beta| \leq r} \int_{V_0'} \left(\mathcal{D}^\beta p_s(x, y, z) \right)^2 (dx, dy, dz), \tag{25}$$

where β is a multi-index, r is the polynomial's order, λ_m is the linear weight. The value set to prevent division by zero of $\epsilon = 10^{-6}$ is used, with $b = 4$ and $\mathcal{D}$ being the derivative operator. The smoothness indicator is a quadratic function of the degrees of freedom (a_k^s) and Eq.(25) can be rewritten as:

$$\mathcal{SI}_s = \sum_{k=1}^{K} a_k^s \left(\sum_{q=1}^{K} \mathcal{OI}_{kq} a_q^s \right), \tag{26}$$

where the oscillation indication matrix $\mathcal{OI}_{kq}$ is given by:

$$\mathcal{OI}_{kq} = \sum_{1 \leq |\beta| \leq r} \int_{V_0'} \left(\mathcal{D}^\beta \phi_k(x, y, z) \right) \left(\mathcal{D}^\beta \phi_q(x, y, z) \right) (dx, dy, dz), \tag{27}$$

which can be precomputed and stored at the beginning of the simulation. For the directional stencils and their corresponding polynomials we employ $r = 1$ to obtain 2nd-order of accuracy, and any arbitrary order of accuracy for the polynomial associated with the central stencil. The

linear weights are computed by firstly assigning the non-normalised linear weight for the central stencil $\lambda_1^{'}$ an arbitrary value, and then normalising this as follows:

$$\lambda_1 = 1 - \frac{1}{\lambda_1^{'}}, \tag{28}$$

with the linear weights associated with lower-order polynomials being equal and provided by the following expression:

$$\lambda_s = \frac{1 - \lambda_1}{s_t - 1}, \tag{29}$$

where s_t is the total number of stencils.

3.4   Troubled-cell indicator

In the context of flows with shocks, material interfaces or other discontinuities, the unlimited DG solution is prone to exhibit oscillations and/or non-linear instabilities. Typically, the DG solution in each cell in the domain is checked with a troubled-cell indicator, designed to flag those cells where certain criteria are violated. In this work we use a detector similar in philosophy to the one developed in [54], which in turn is based on the KXRCF indicator [55] developed on the DG superconvergence property argument. The modification we propose with respect to [54] is to cell-average the solution of the neighbouring cells over the respective cell and not over the target cell like in [54]. This results in the following:

$$\frac{\sum_{n=1}^{N} \left| \frac{1}{\Omega_0} \int_{\Omega_0} u_0(x,y,z) dV - \frac{1}{\Omega_n} \int_{\Omega_n} u_n(x,y,z)) dV \right|}{\max_{n \in \{0...N\}} \left\{ \frac{1}{\Omega_n} \left| \int_{\Omega_n} u_n(x,y,z) dV \right| \right\}} > C_k \tag{30}$$

where the threshold value C_k is usually taken to be 0.1 and the detector is applied to density and energy variables only, unless otherwise specified.

4   RESULTS AND DISCUSSION

4.0.1   Multi-species convergence test

For verifying the designed order of spatial accuracy for the numerical schemes developed, a multi-species advection test similar to the one employed by Wong and Lele [56] is used. In this test a smooth volume fraction initial profile of two gases is advected for ten periods in a periodic computational domain. The initial condition is given by:

$$(\rho_1, \rho_2, u, v, p, a_1) = (7, 1, 1, 0, 1/1.4, 0.5 + 0.25 \sin(2\pi(x - 0.5))). \tag{31}$$

The 2D computational domain is defined by $[0,1]^2$, and the problem is run on three different type of meshes: a uniform quadrilateral mesh, an unstructured triangular mesh as in figure Fig.(1)(a) and a hybrid mesh consisting of arbitrary quadrilateral and triangular elements as in figure Fig.(1)(b), each with 16, 32, 64 and 128 edges per side resolution. The simulation is run for a time of $t_f = 10$ and the two gases selected are nitrogen and helium with specific heats 1.4 and 1.66 respectively. The numerical errors e_{L^2} and the e_{L^∞} are computed as follows:

$$e_{L^2} = \sqrt{\frac{\sum_i \int_{\Omega_i} (\mathbf{U}_e(x, t_f) - \mathbf{U}_c(x, t_f))^2 dV}{\sum_i |\Omega_i|}}, \tag{32}$$
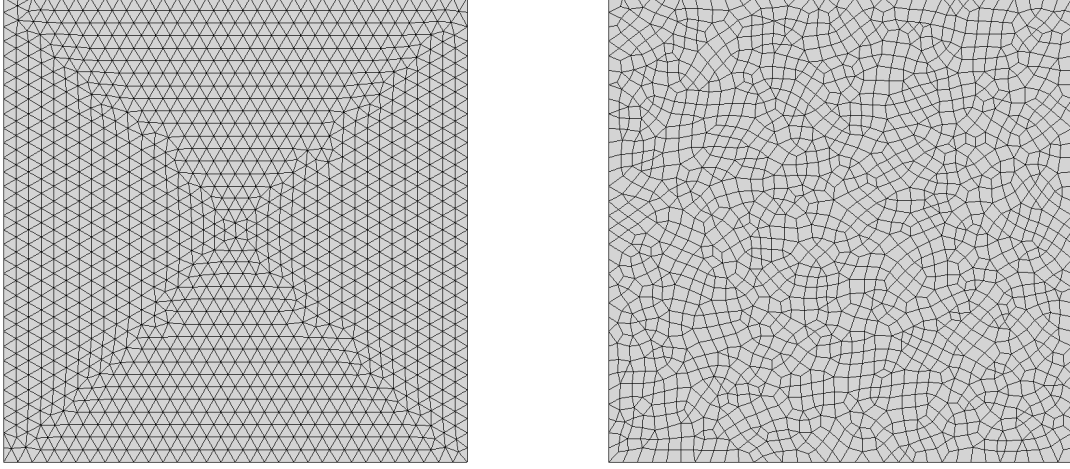
(a) Triangular mesh   (b) Hybrid mesh

Figure 1: Computed results for the solid body rotation on hybrid mesh with 64 edges per side with 3rd order polynomial.

$$e_{L\infty} = \mathcal{M}ax \left| \left(\mathbf{U}_e \left(x, t_f \right) - \mathbf{U}_c \left(x, t_f \right) \right| \right., \tag{33}$$

where $\mathbf{U}_c \left(x, t_f \right)$ and $\mathbf{U}_e \left(x, t_f \right)$ are the computed and exact solutions at the end of the simulation $t_f = 10.0$. The exact solution $\mathbf{U}_e \left(x, t_f \right)$ being given by the initial condition itself at $t = 0$. The results are listed in table Tab.(1) for all meshes and polynomials $\mathcal{P}2$ and $\mathcal{P}3$, corresponding to a formal 3rd and 4th order respectively. The error norms for volume fraction of species 1, a_1, and mass fraction of species 1, $a_1 \rho_1$, are close to the target theoretical order of convergence, and the latter variable is overall slightly more accurate on all meshes and discretisation orders.

4.1   Isolated material interface advection

For assessing the non-oscillatory properties of the considered schemes, the advection of a sharp material interface within a periodic domain is considered. A sharp material interface is frequently encountered in several multicomponent flows, hence the robustness of the proposed methods is of paramount importance, for the successful deployment of these schemes in multicomponent flows. The material interface is advected with constant velocity across the computational domain, and the pressure and temperature is also constant across the interface. The initial conditions are given by:

$$\left(\rho, u, v, p, \gamma, a_1 \right) = \begin{cases} \left(10.0, 0.5, 0, 1/1.4, 1.4, 1 \right), & \text{if } x < 0.5 \\ \left(1.0, 0.5, 0, 1/1.4, 1.66, 0 \right), & \text{otherwise.} \end{cases} \tag{34}$$

The problem is solved on three type of meshed defined on a 2D computational domain defined, again, by $[0, 1]^2$. A uniform quadrilateral, as well as unstructured triangular and hybrid meshes are tested, as shown in Fig.(1), each with 32 edges per side resolution, and the simulation is run

Table 1: Values for $e_{L\infty}$ and e_{L^2} error norms and convergence rates for the volume fraction and mass fraction of species 1, a_1 and $a_1\rho_1$ respectively, computed with the hybrid FV/DG scheme on uniform and unstructured meshes at the final time t=10.0.

| Order/Number of Edges	a_1				$a_1\rho_1$			
Quadrilateral Mesh	$e_{L\infty}$	$\mathcal{O}_{L\infty}$	e_{L^2}	$\mathcal{O}_{L^2}$	$e_{L\infty}$	$\mathcal{O}_{L\infty}$	e_{L^2}	$\mathcal{O}_{L^2}$
$\mathcal{P}2/16$	1.79E-02	-	1.07E-02	-	3.66E-03	-	1.75E-03	-
$\mathcal{P}2/32$	2.38E-03	2.91	1.48E-03	2.85	5.44E-04	2.75	2.44E-04	2.84
$\mathcal{P}2/64$	3.15E-04	2.92	1.84E-04	3.01	7.46E-05	2.87	2.98E-05	3.04
$\mathcal{P}2/128$	3.62E-05	3.12	2.30E-05	3.00	9.42E-06	2.98	3.76E-06	2.99
$\mathcal{P}3/16$	5.26E-03	-	2.56E-03	-	1.34E-03	-	3.61E-04	-
$\mathcal{P}3/32$	3.23E-04	4.03	1.18E-04	4.44	8.24E-05	4.02	2.35E-05	3.94
$\mathcal{P}3/64$	3.24E-05	3.32	8.29E-06	3.83	7.16E-06	3.52	1.63E-06	3.85
$\mathcal{P}3/128$	1.99E-06	4.03	5.21E-07	3.99	4.66E-07	3.94	9.79E-08	4.06
Triangular Mesh	$e_{L\infty}$	$\mathcal{O}_{L\infty}$	e_{L^2}	$\mathcal{O}_{L^2}$	$e_{L\infty}$	$\mathcal{O}_{L\infty}$	e_{L^2}	$\mathcal{O}_{L^2}$
$\mathcal{P}2/16$	2.90E-03	-	1.77E-03	-	3.03E-03	-	3.73E-04	-
$\mathcal{P}2/32$	3.92E-04	2.89	2.40E-04	2.88	4.28E-04	2.83	5.58E-05	2.74
$\mathcal{P}2/64$	4.91E-05	2.99	3.08E-05	2.96	5.17E-05	3.05	7.49E-06	2.90
$\mathcal{P}2/128$	6.03E-06	3.03	3.85E-06	3.00	7.12E-06	2.86	8.52E-07	3.14
$\mathcal{P}3/16$	1.84E-04	-	6.85E-05	-	6.47E-05	-	1.55E-05	-
$\mathcal{P}3/32$	1.35E-05	3.77	4.70E-06	3.87	6.36E-06	3.35	1.15E-06	3.75
$\mathcal{P}3/64$	8.04E-07	4.07	2.87E-07	4.03	4.28E-07	3.89	8.01E-08	3.85
$\mathcal{P}3/128$	5.90E-08	3.77	1.95E-08	3.88	2.92E-08	3.87	5.36E-09	3.90
Hybrid Mesh	$e_{L\infty}$	$\mathcal{O}_{L\infty}$	e_{L^2}	$\mathcal{O}_{L^2}$	$e_{L\infty}$	$\mathcal{O}_{L\infty}$	e_{L^2}	$\mathcal{O}_{L^2}$
$\mathcal{P}2/16$	7.73E-03	-	4.31E-03	-	2.01E-03	-	7.44E-04	-
$\mathcal{P}2/32$	1.00E-03	2.95	5.23E-04	3.04	2.47E-04	3.02	8.80E-05	3.08
$\mathcal{P}2/64$	1.14E-04	3.14	6.24E-05	3.07	2.94E-05	3.07	1.07E-05	3.05
$\mathcal{P}2/128$	1.51E-05	2.92	7.66E-06	3.03	3.98E-06	2.88	1.32E-06	3.02
$\mathcal{P}3/16$	7.49E-04	-	2.38E-04	-	3.02E-04	-	6.29E-05	-
$\mathcal{P}3/32$	5.64E-05	3.73	1.39E-05	4.10	2.21E-05	3.77	3.98E-06	3.98
$\mathcal{P}3/64$	3.61E-06	3.97	6.85E-07	4.34	1.96E-06	3.50	2.58E-07	3.94
$\mathcal{P}3/128$	1.99E-07	4.18	4.52E-08	3.98	1.50E-07	3.70	1.91E-08	3.76

for a time of $t_f = 2$. The adopted scheme is a 3rd order DG scheme with 3rd order CWENOZ reconstruction for the troubled cells.

From figure Fig.(2) is clear how the improved accuracy of the hybrid FV/DG schem, is beneficial for reducing the numerical dissipation, and resulting in a less smeared material interface at the final time compared to the pure FV method. The reconstruction on primitive variable also results in uniform velocity and pressure solutions, and free of oscillations, as confirmed by the normalised pressure error which is close to machine precision.
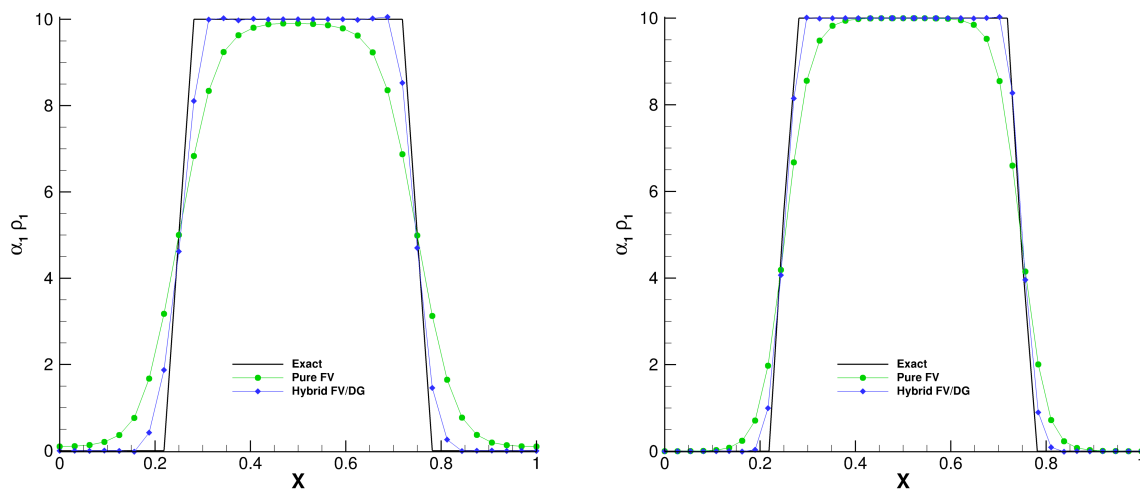
(a) Quadrilateral mesh

(b) Triangular mesh
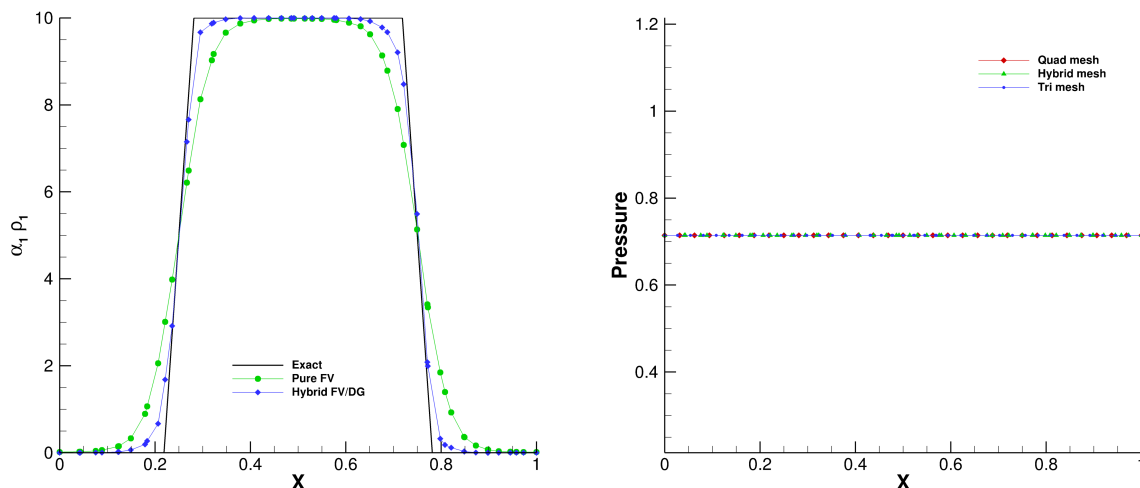
(c) Hybrid mesh

(d) Pressure plot

Figure 2: Computed results for the solid body rotation on hybrid mesh with 64 edges per side with 3rd order polynomial.

4.2 Helium bubble - shock wave interaction

The interaction of a weak shockwave in air and a helium bubble is considered in 2D. Several variations of this test problem have been widely used [6,57,58] for assessing the performance of several techniques for multicomponent flow modelling, and is based on the experimental setup by Haas and Sturtevant [59]. A bubble of diameter $D_b = 5cm$, is placed within an air filled shock tube. The bubble consists of helium and air of 28% mass concentration. A shockwave moving
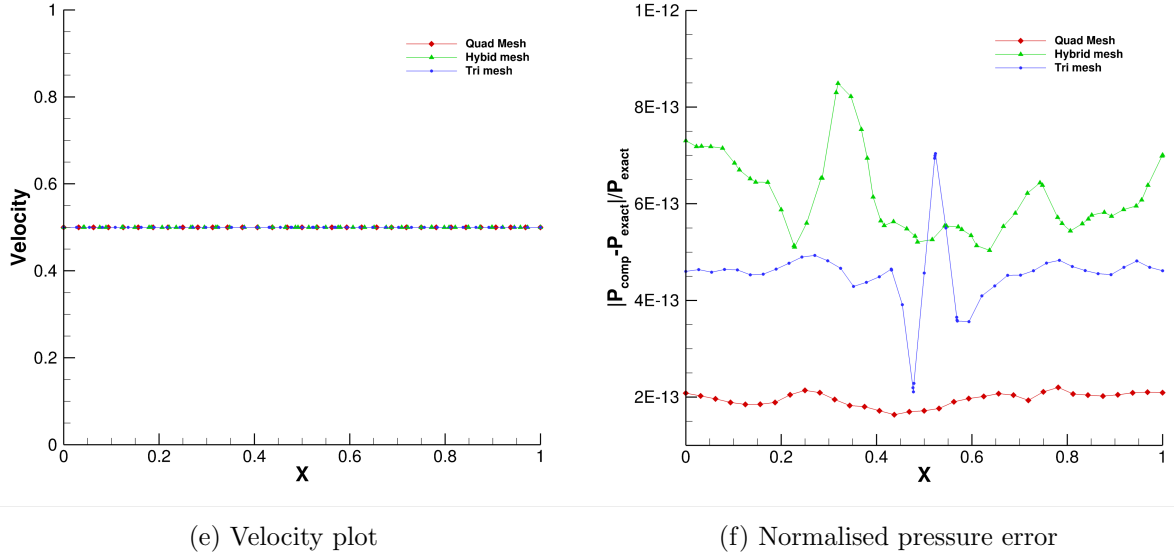
(e) Velocity plot
(f) Normalised pressure error

Figure 2: Computed results for the solid body rotation on hybrid mesh with 64 edges per side with 3rd order polynomial.

from right to left of the setup impacts the bubble contaminated by the surrounding air. The specific heats of 1.4 and 1.66 are used for air and helium, respectively, and the initial condition is given by:

$$(a_1\rho_1, a_2\rho_2, u, v, p, a_1) = \begin{cases} (0.0, 1.204, 0, 0, 101325, 0), & \text{for Pre-shock} \\ (0.0, 1.658, -114.49, 0, 159060, 0), & \text{for Post-shock} \\ (0.158, 0.061, 0, 0, 101325, 0.95), & \text{for Bubble.} \end{cases} \quad (35)$$

The computation domain is discretised by a hybrid unstructured mesh consisting of quadrilateral and triangular elements for a total count of $\approx 250k$ elements, and a 3rd order DG scheme with 3rd order CWENOZ reconstruction, namely $\mathcal{P}2 - CWENOZ3$, is adopted. The sequence in Fig.(3) illustrates the initial instants of the shock wave interaction with the material interface up to time $t = 517\mu s$. Thanks to the reduced dissipation of the scheme, the initial material interface is only slightly diffused, and it is also possible to observe the onset of instabilities at the interface.

5 CONCLUSIONS

This work presented a hybrid DG/FV framework for the solution of multi-species flows with an attempt at reducing the interface smearing of the material interface typical of diffuse-interface models. The five-equation diffuse-interface model of Allaire et al. [1] is solved with a modal DG scheme in smooth flow regions, and a troubled cell indicator detects the region with discontinuous features such material interfaces and shock waves. For the cells deemed as troubled, a FV type reconstruction is activated following the CWENOZ paradigm, reducing the computational costs and increasing the robustness of the classic WENO schemes. The reconstruction is performed on
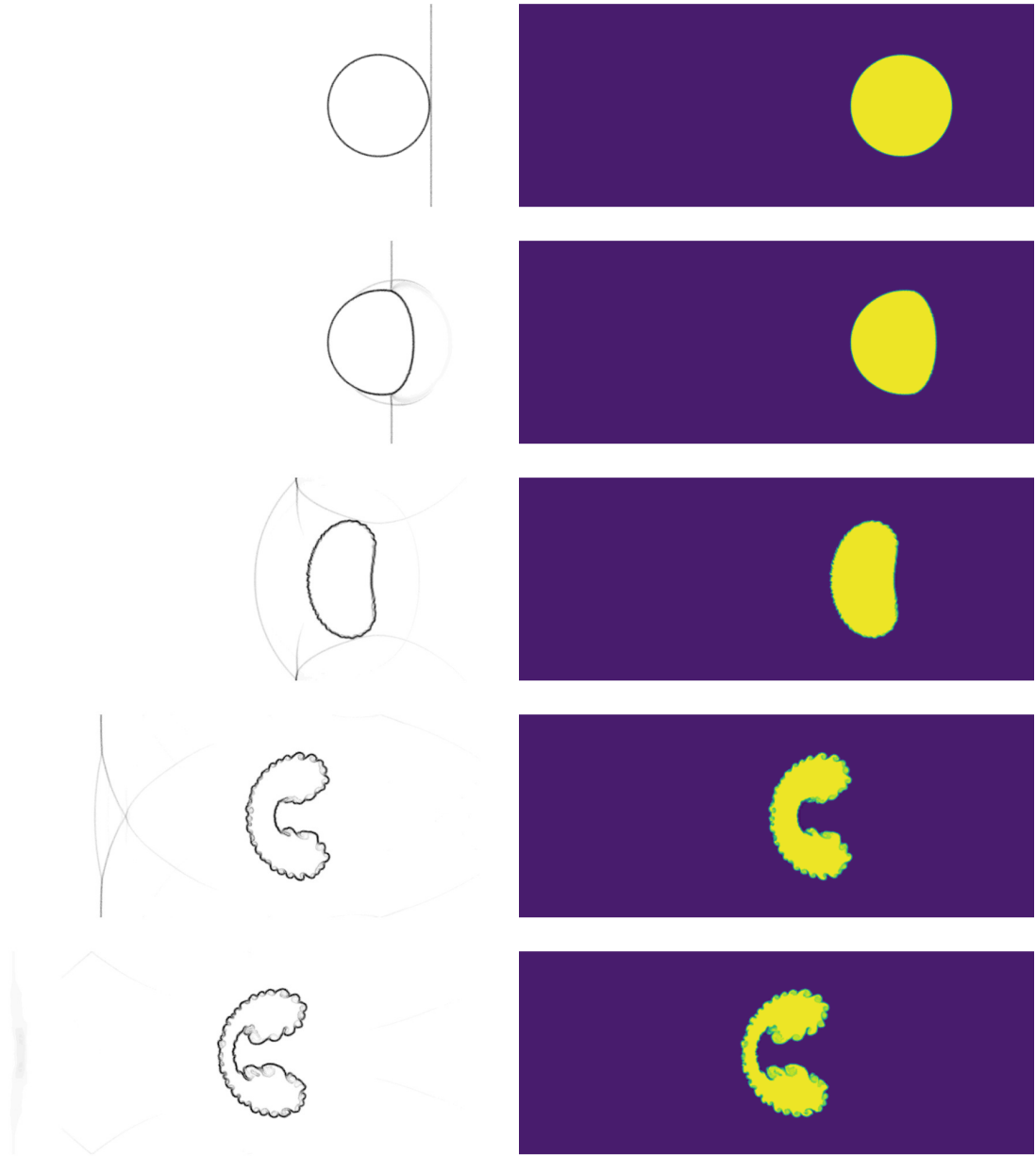
Figure 3: Density gradient magnitude (left) and volume fraction contours (right) for helium bubble-shock wave interaction for times $t = 57\mu s$, $t = 104\mu s$, $t = 208\mu s$, $t = 417\mu s$ and $t = 517\mu s$ from top to bottom respectively

primitive variables in order to avoid oscillation at interfaces as shown in the results section, and the higher accuracy provided by the DG discretisation is beneficial to avoid excessive interface smearing. Future developments will aim to extend the present framework to non-equilibrium models and will seek for ad-hoc troubled cell indicators for multi-species flow problems.

REFERENCES

[1] G. Allaire, S. Clerc, S. Kokh, A five-equation model for the simulation of interfaces between compressible fluids, Journal of Computational Physics 181 (2) (2002) 577–616. doi:10.1006/jcph.2002.7143.

[2] R. Saurel, C. Pantano, Diffuse-Interface Capturing Methods for Compressible Two-Phase Flows, Annual Review of Fluid Mechanics 50 (1) (2018) 105–130. URL https://hal.archives-ouvertes.fr/hal-02115896

[3] V. Maltsev, M. Skote, P. Tsoutsanis, High-order methods for diffuse-interface models in compressible multi-medium flows: A review, Physics of Fluids 34 (2) (2022). doi:10.1063/5.0077314.

[4] R. Borges, M. Carmona, B. Costa, W. S. Don, An improved weighted essentially non-oscillatory scheme for hyperbolic conservation laws, Journal of Computational Physics 227 (6) (2008) 3191–3211. doi:10.1016/j.jcp.2007.11.038.

[5] P. Tsoutsanis, M. Dumbser, Arbitrary high order central non-oscillatory schemes on mixed-element unstructured meshes, Computer and Fluids 225 (2021). doi:10.1016/j.compfluid.2021.104961.

[6] E. Johnsen, T. Colonius, Implementation of WENO schemes in compressible multi-component flow problems, Journal of Computational Physics 219 (2) (2006) 715–732. doi:10.1016/j.jcp.2006.04.018.

[7] C. Hirt, B. Nichols, Volume of Fluid (VOF) Method for the Dynamics of Free Boundaries, Journal of Computational Physics (1981) 357–.

[8] E. Olsson, G. Kreiss, A conservative level set method for two phase flow, Journal of Computational Physics 210 (1) (2005) 225–246. doi:10.1016/j.jcp.2005.04.007.

[9] R. P. Fedkiw, T. Aslam, S. Xu, The Ghost Fluid Method for Deflagration and Detonation Discontinuities, Journal of Computational Physics 154 (2) (1999) 393–427. doi:10.1006/jcph.1999.6320.

[10] S. O. Unverdi, G. Tryggvason, A front-tracking method for viscous, incompressible, multi-fluid flows, Journal of Computational Physics 100 (1) (1992) 25–37. doi:10.1016/0021-9991(92)90307-K.

[11] J. Glimm, J. W. Grove, X. L. Li, K. M. Shyue, Y. Zeng, Q. Zhang, Three-dimensional front tracking, SIAM Journal of Scientific Computing 19 (3) (1998) 703–727. doi:10.1137/S1064827595293600.

[12] M. R. Baer, J. W. Nunziato, A Two-Phase Mixture Theory For The Deflagration-to-Detonation Transition (DDT) in Reactive Granular Materials, Int.J. Multiphase Flow 12 (6) (1986) 861–889.

[13] R. Abgrall, How to prevent pressure oscillations in multicomponent flow calculations: A quasi conservative approach, Journal of Computational Physics 125 (1) (1996) 150–160. doi:10.1006/jcph.1996.0085.

[14] A. K. Kapila, R. Menikoff, J. B. Bdzil, S. F. Son, D. S. Stewart, Two-phase modeling of deflagration-to-detonation transition in granular materials: Reduced equations, Physics of Fluids 13 (10) (2001) 3002–3024. doi:10.1063/1.1398042.

[15] S. K. Godunov, E. I. Romenskii, Nonstationary equations of nonlinear elasticity theory in eulerian coordinates, Journal of Applied Mechanics and Technical Physics 13 (6) (1972) 868–884. doi:10.1007/BF01200547.

[16] I. Peshkov, E. Romenski, A hyperbolic model for viscous Newtonian flows, Continuum Mechanics and Thermodynamics 28 (1-2) (2016) 85–104. doi:10.1007/s00161-014-0401-6.

[17] N. Favrie, S. L. Gavrilyuk, Diffuse interface model for compressible fluid - Compressible elastic-plastic solid interaction, Journal of Computational Physics 231 (7) (2012) 2695–2723. doi:10.1016/j.jcp.2011.11.027.
URL http://dx.doi.org/10.1016/j.jcp.2011.11.027

[18] S. L. Gavrilyuk, N. Favrie, R. Saurel, Modelling wave dynamics of compressible elastic materials, Journal of Computational Physics 227 (5) (2008) 2941–2969. doi:10.1016/j.jcp.2007.11.030.

[19] K. K. So, X. Y. Hu, N. A. Adams, Anti-diffusion interface sharpening technique for two-phase compressible flow simulations, Journal of Computational Physics 231 (11) (2012) 4304–4323. doi:10.1016/j.jcp.2012.02.013.

[20] R. K. Shukla, C. Pantano, J. B. Freund, An interface capturing method for the simulation of multi-phase compressible flows, Journal of Computational Physics 229 (19) (2010) 7411–7439. doi:10.1016/j.jcp.2010.06.025.
URL http://dx.doi.org/10.1016/j.jcp.2010.06.025

[21] A. Tiwari, J. B. Freund, C. Pantano, A diffuse interface model with immiscibility preservation, Journal of Computational Physics 252 (2013) 290–309. doi:10.1016/j.jcp.2013.06.021.
URL http://dx.doi.org/10.1016/j.jcp.2013.06.021

[22] E. Franquet, V. Perrier, Runge-Kutta discontinuous Galerkin method for the approximation of Baer and Nunziato type multiphase models, Journal of Computational Physics 231 (11) (2012) 4096–4141. doi:10.1016/j.jcp.2012.02.002.

[23] L. D. Gryngarten, S. Menon, A generalized approach for sub- and super-critical flows using the Local Discontinuous Galerkin method, Computer Methods in Applied Mechanics and Engineering 253 (2013) 169–185. doi:10.1016/j.cma.2012.08.021.
URL http://dx.doi.org/10.1016/j.cma.2012.08.021

[24] P. Tsoutsanis, E. M. Adebayo, A. Carriba Merino, A. Perez Arjona, M. Skote, CWENO finite-volume interface capturing schemes for multicomponent flows using unstructured meshes, Journal of Scientific Computing 89 (2021). doi:10.1007/s10915-021-01673-y.

[25] UCNS3D CFD code, `http://www.ucns3d.com`, accessed: 2022-05-05.

[26] A. F. Antoniadis, D. Drikakis, P. S. Farmakis, L. Fu, I. Kokkinakis, X. Nogueira, P. A. S. F. Silva, M. Skote, V. Titarev, P. Tsoutsanis, UCNS3D : An open-source high-order finite-volume unstructured CFD, Computer Physics Communications 279 (2022) 108453. doi:10.1016/j.cpc.2022.108453.
URL `https://doi.org/10.1016/j.cpc.2022.108453`

[27] B. Cockburn, C.-w. Shu, TVB Runge-Kutta projection discontinous Galerkin finite element methodsII.pdf (1989).

[28] B. Cockburn, S. Y. Lin, C. W. Shu, TVB runge-kutta local projection discontinuous galerkin finite element method for conservation laws III: One-dimensional systems, Journal of Computational Physics 84 (1) (1989) 90–113. doi:10.1016/0021-9991(89)90183-6.

[29] D. A. Di Pietro, A. Ern, Mathematical Aspects of Discontinuous Galerkin Methods, Springer Heidelberg Dordrecht London New York, 2011.

[30] W. Boscheri, G. Dimarco, High order modal Discontinuous Galerkin Implicit–Explicit Runge Kutta and Linear Multistep schemes for the Boltzmann model on general polygonal meshes, Computers and Fluids 233 (October 2021) (2022) 105224. doi:10.1016/j.compfluid.2021.105224.
URL `https://doi.org/10.1016/j.compfluid.2021.105224`

[31] P. Tsoutsanis, V. Titarev, D. Drikakis, WENO schemes on arbitrary mixed-element unstructured meshes in three space dimensions, Journal of Computational Physics 230 (4) (2011) 1585–1601.

[32] E. F. Toro, M. Spruce, W. Speares, Restoration of the contact surface in the HLL-Riemann solver, Shock Waves 4 (1) (1994) 25–34. doi:10.1007/BF01414629.

[33] S. Gottlieb, C.-W. Shu, Total variation diminishing Runge-Kutta schemes, Mathematics of Computation 67 (221) (1998) 73–85. doi:10.1090/s0025-5718-98-00913-2.

[34] P. Tsoutsanis, A. Antoniadis, D. Drikakis, WENO schemes on arbitrary unstructured meshes for laminar, transitional and turbulent flows, Journal of Computational Physics 256 (2014) 254–276.

[35] V. Titarev, P. Tsoutsanis, D. Drikakis, WENO schemes for mixed-element unstructured meshes, Communications in Computational Physics 8 (3) (2010) 585–609.

[36] P. Tsoutsanis, D. Drikakis, A high-order finite-volume method for atmospheric flows on unstructured grids, Journal of Coupled Systems and Multiscale Dynamics 4 (2016) 170–186. doi:10.1166/jcsmd.2016.1104.

[37] A. Antoniadis, P. Tsoutsanis, D. Drikakis, Numerical accuracy in RANS computations of high-lift multi-element airfoil and aircraft configurations, in: 53rd AIAA Aerospace Sciences Meeting, Vol. 0317, 2015. doi:10.2514/6.2015-0317.

[38] A. Antoniadis, P. Tsoutsanis, D. Drikakis, High-order schemes on mixed-element unstructured grids for aerodynamic flows, in: 42nd AIAA Fluid Dynamics Conference and Exhibit, Vol. 2833, 2012. doi:10.2514/6.2012-2833.

[39] A. Antoniadis, P. Tsoutsanis, I. Kokkinakis, Z. Rana, D. Drikakis, Azure: An advanced CFD software suite based on high-resolution and high-order methods, in: 53rd AIAA Aerospace Sciences Meeting, Vol. 0813, 2015. doi:10.2514/6.2015-0813.

[40] A. Antoniadis, D. Drikakis, I. W. Kokkinakis, P. Tsoutsanis, Z. Rana, High-order methods for hypersonic shock wave turbulent boundary layer interaction flow, in: 20th AIAA International Space Planes and Hypersonic Systems and Technologies Conference, Vol. 3524, 2015. doi:10.2514/6.2015-3524.

[41] P. Tsoutsanis, I. Kokkinakis, L. Konozsy, D. Drikakis, R. Williams, D. Youngs, Comparison of structured- and unstructured-grid, compressible and incompressible methods using the vortex pairing problem, Computer Methods in Applied Mechanics and Engineering 293 (2015) 207–231. doi:10.1016/j.cma.2015.04.010.

[42] P. Tsoutsanis, H. Srinivasan, Adaptive mesh refinement techniques for high-order finite-volume WENO schemes, in: ECCOMAS Congress 2016, Crete, Greece, 2016. doi:10.7712/100016.2003.8544.

[43] P. Tsoutsanis, N. Simmonds, A. Gaylard, Implementation of a low-Mach number modification for high-order finite-volume schemes for arbitrary hybrid unstructured meshes, in: ECCOMAS Congress 2016, Crete, Greece, 2016. doi:10.7712/100016.2004.8545.

[44] P. Tsoutsanis, D. Drikakis, Addressing the challenges of implementation of high-order finite-volume schemes for atmospheric dynamics on unstructured meshes, in: ECCOMAS Congress 2016, Crete, Greece, 2016. doi:10.7712/100016.1846.8406.

[45] P. Tsoutsanis, A. Antoniadis, K. Jenkins, Improvement of the computational performance of a parallel unstructured WENO finite volume CFD code for implicit large eddy simulation, Computers and Fluids 173 (2018) 157–170. doi:10.1016/j.compfluid.2018.03.012.

[46] P. Farmakis, P. Tsoutsanis, X. Nogueira, WENO schemes on unstructured meshes using a relaxed a posteriori MOOD limiting approach, Computer Methods in Applied Mechanics and Engineering 363 (2020). doi:10.1016/j.cma.2020.112921.

[47] P. Tsoutsanis, Extended bounds limiter for high-order finite-volume schemes on unstructured meshes, Journal of Computational Physics 362 (2018) 69–94.

[48] N. Simmonds, P. Tsoutsanis, A. Antoniadis, K. Jenkins, A. Gaylard, Low-Mach number treatment for finite-volume schemes on unstructured meshes, Applied Mathematics and Computation 336 (2018) 368–393.

[49] F. Ricci, P. Silva, P. Tsoutsanis, A. Antoniadis, Hovering rotor solutions by high-order methods on unstructured grids, Aerospace Science and Technology 97 (2020). doi:10.1016/j.ast.2019.105648.

[50] P. Silva, P. Tsoutsanis, A. Antoniadis, Simple multiple reference frame for high-order solution of hovering rotors with and without ground effect, Aerospace Science and Technology 111 (2021). doi:10.1016/j.ast.2021.106518.

[51] P. Tsoutsanis, Stencil selection algorithms for WENO schemes on unstructured meshes, Journal of Computational Physics: X 4 (2019). doi:10.1016/j.jcpx.2019.100037.

[52] A. F. Antoniadis, P. Tsoutsanis, D. Drikakis, Assessment of high-order finite volume methods on unstructured meshes for rans solutions of aeronautical configurations, Computers and Fluids 146 (2017) 86–104. doi:https://doi.org/10.1016/j.compfluid.2017.01.002.

[53] M. Castro, B. Costa, W. S. Don, High order weighted essentially non-oscillatory WENO-Z schemes for hyperbolic conservation laws, Journal of Computational Physics 230 (5) (2011) 1766–1792. doi:10.1016/j.jcp.2010.11.028.
URL http://dx.doi.org/10.1016/j.jcp.2010.11.028

[54] G. Fu, C. W. Shu, A new troubled-cell indicator for discontinuous Galerkin methods for hyperbolic conservation laws, Journal of Computational Physics 347 (2017) 305–327. doi:10.1016/j.jcp.2017.06.046.
URL http://dx.doi.org/10.1016/j.jcp.2017.06.046

[55] L. Krivodonova, J. Xin, J. F. Remacle, N. Chevaugeon, J. E. Flaherty, Shock detection and limiting with discontinuous Galerkin methods for hyperbolic conservation laws, Applied Numerical Mathematics 48 (3-4) (2004) 323–338. doi:10.1016/j.apnum.2003.11.002.

[56] M. L. Wong, S. K. Lele, High-order localized dissipation weighted compact nonlinear scheme for shock- and interface-capturing in compressible flows, Vol. 339, Elsevier Inc., 2017. arXiv:1701.08905, doi:10.1016/j.jcp.2017.03.008.
URL http://dx.doi.org/10.1016/j.jcp.2017.03.008

[57] Q. Wang, R. Deiterding, J. Pan, Y. X. Ren, Consistent high resolution interface-capturing finite volume method for compressible multi-material flows, Computers and Fluids 202 (2020) 104518. doi:10.1016/j.compfluid.2020.104518.
URL https://doi.org/10.1016/j.compfluid.2020.104518

[58] V. Coralic, T. Colonius, Finite-volume WENO scheme for viscous compressible multicomponent flows, Journal of Computational Physics 274 (2014) 95–121. doi:10.1016/j.jcp.2014.06.003.
URL http://dx.doi.org/10.1016/j.jcp.2014.06.003

[59] J. F. Haas, B. Sturtevant, Interaction of Weak Shock Waves With Cylindrical And Spherical Gas Inhomogeneities, Journal of Fluid Mechanics 181 (1987) 41–76. doi:10.1017/S0022112087002003.